

Numerical Heat Transfer, Part B: Fundamentals



ISSN: 1040-7790 (Print) 1521-0626 (Online) Journal homepage: http://www.tandfonline.com/loi/unhb20

Heat and Mass Transfer in Moist Soil, Part II. Application to Predicting Thermal Signatures of Buried Landmines

F. Moukalled, N. Ghaddar, Y. Saleh & Z. Fawaz

To cite this article: F. Moukalled, N. Ghaddar, Y. Saleh & Z. Fawaz (2006) Heat and Mass Transfer in Moist Soil, Part II. Application to Predicting Thermal Signatures of Buried Landmines, Numerical Heat Transfer, Part B: Fundamentals, 49:5, 487-512

To link to this article: http://dx.doi.org/10.1080/10407790500510965

	Published online: 24 Feb 2007.
	Submit your article to this journal $oldsymbol{\mathcal{C}}$
ılıl	Article views: 49
a ^L	View related articles 🗗
4	Citing articles: 3 View citing articles 🗷

Full Terms & Conditions of access and use can be found at http://www.tandfonline.com/action/journalInformation?journalCode=unhb20

Copyright © Taylor & Francis Group, LLC ISSN: 1040-7790 print/1521-0626 online

DOI: 10.1080/10407790500510965



HEAT AND MASS TRANSFER IN MOIST SOIL, PART II. APPLICATION TO PREDICTING THERMAL SIGNATURES OF BURIED LANDMINES

F. Moukalled, N. Ghaddar, and Y. Saleh

Department of Mechanical Engineering, American University of Beirut, Riad El Solh, Beirut, Lebanon

Z. Fawaz

Ryerson University, School of Aerospace Engineering, Toronto, Canada

The finite-volume-based numerical procedure for unsteady heat and moisture transport in soil developed in a companion article [1] is used to study the surface thermal signature of buried landmines in moist soil. The effect of soil type, soil moisture content, mine type, and mine burial depth on the thermal contrast at the soil surface is analyzed over a diurnal cycle. Predictions are presented in the form of spatial and temporal profiles of temperature, matric potential, and surface thermal contrast. Results reveal that the thermal contrast at the surface becomes weaker as the burial depth increases. For shallowly buried mines (i.e., buried at a depth of less than 2 cm), there is an optimum matric potential or moisture content value that maximizes the thermal contrast at the soil surface, with this value being highly dependent on the type of soil and/or mine. Varying the mine burial depth and/or soil moisture content changes the time of the day at which this maximum thermal contrast occurs.

INTRODUCTION

Landmines are detected mainly using metal detector devices, which is a very slow, hazardous, and costly approach. In addition, many types of mines are made of plastic or wood, rendering them invisible to metal detectors. Researchers are working to find better ways to detect landmines, which not only address the existing problem but also have the potential of making the placement of new landmines less attractive. At present, this effort has met with technical and economic difficulties, due to the near-perfect rate of detection required. Several technologies for detecting landmines have been tried (infrared imaging [2], ground-penetrating radar [3], tracevapor explosive detection [4], nuclear methods [5], etc.), but none of them has been able to perform with perfect accuracy. Infrared (IR) imaging is a promising low-cost

Received 27 June 2005; accepted 8 November 2005.

Financial support provided by the Lebanese National Council for Scientific Research (LNCSR) through Grant LCR-11304-002208 and by Mr. Youssef Jameel through Grant DCU 113010-024021 is gratefully acknowledged.

Address correspondence to F. Moukalled, Department of Mechanical Engineering, American University of Beirut, P.O. Box 11-0236, Riad El Solh, Beirut 1107 2020, Lebanon. E-mail: memouk@aub.edu.lb

NOMENCLATURE						
C	ground albedo	q'''	heat generation, W/m ³			
C_L	cloud cover	$r_a, r_s, r_{\text{total}}$	aerodynamic, surface, and total			
C_P	specific heat capacity, J/kg K		surface resistance to mass transfer,			
$C_{T\psi}$	thermal total moisture capacitance		s/m			
·	terms, K ⁻¹	S_o	solar constant, W/m ²			
$C_{\psi T}, C_{TT}$	matric, J/m^4 , and thermal, $J/m^3 K$,	t	time, s			
	heat capacitance terms	T	temperature, K			
$C_{\psi v}, C_{\psi \psi}$	matric vapor and total moisture	Z	vertical distance, m			
	capacitance terms, m ⁻¹	α	thermal diffusivity, m ² /s			
D_a	molecular diffusivity of water vapor	δ	declination angle			
	in air, m ² /s	θ	volumetric moisture content, m ³ /m ³			
D_h	heat diffusivity in air, m/s	ξ	temperature gradient ratio			
$D_{T\psi}$	thermal total moisture diffusivity,	ρ	density, kg/m ³			
	$m^2/s K$	ф	zenith angle			
D_v	vapor diffusivity in air, m/s	ψ	matric liquid potential (pressure			
$D_{\psi T}$	matric potential heat diffusivity,		head), m			
	W/m^2	Φ	total soil matric potential for liquid			
$D_{\psi v}, D_{\psi \psi}$	matric vapor and total moisture diffusivities, m/s		flow, m			
h	convective heat transfer coefficient,	Subscripts				
	$W/m^2 K$	air	ambient air			
h_{fg}	latent heat of vaporization of water,	g	ground			
30	J/kg	i	initial value			
k	effective thermal conductivity,	1	liquid			
	W/m K	m	mine			
K	hydraulic conductivity of soil, m/s	S	saturated, surface			
m	mass flow rate, kg/m ² s	v	vapor			
$M(\phi)$	atmospheric transmissivity	VS	saturated vapor			
n	outward unit vector	w	water, wind			

technology, which has the potential to be used in conjunction with other existing technologies for mine detection. With this technology, thermal images of the soil surface are captured using an IR camera that can detect light in the infrared range and convert it into corresponding temperature variations. As objects of dissimilar thermal capacitance absorb and release heat at different rates, a buried landmine heats up and cools down at a rate different from the surrounding soil. This unequal heat transfer rate manifests itself on the surface above the mine through either a higher or a lower soil surface temperature than the surface temperature at a location away from the mine. This variation in temperature is denoted in the literature by "thermal signature" [6–9] and appears as a thermal contrast in an image taken by an IR camera.

Several investigators have used IR technology as a tool for detecting buried landmines. However, most of the reported work has been directed either toward developing the signal processing algorithms or toward finding ways to enhance the thermal signature of the landmine. Simard [2] investigated experimentally, using passive IR imaging, ways to improve landmine detection capability. Larive et al. [10] developed a preprocessing algorithm to help the discrimination between natural and man-made objects. Filippidis et al. [11] used an IR sensor sensitive to polarization in order to highlight the signature of man-made targets, such as landmines,

relying on natural features in the image. Janssen et al. [7] examined the time development for buried and surface-laid mines, and concluded that the surface-laid objects are visible throughout the whole diurnal cycle, while the buried ones are visible only during sunrise and sunset. Bruschini and Gros [12] assessed the potential of using IR imaging for landmine detection, described its advantages and limitations, and estimated that IR images can reflect the presence of a mine buried up to a maximum depth of 10-15 cm. It was further indicated that the results of IR imaging depend heavily on environmental conditions. In a recent article, Deans et al. [13] reported on an experimental investigation using thermal imaging with microwave heating to enhance the visibility of a buried landmine. Their measurements indicated that mines buried in dry sand can be observed up to a burial depth of 2 cm, which departs significantly from the 10-15 cm mentioned by Bruschini and Gros [12]. It is speculated that this difference in buried depth within which landmines are detectable by an IR sensor is possibly due to the different types of soil used. Hermann and Chant [14], using IR sensors, investigated experimentally the enhancement of the thermal signature of buried landmines through volumetric heating via microwave energy sources. The authors also presented a one-dimensional model for microwave absorption and heat dissipation by moisture-laden soils in the presence of a surrogate buried landmine. Mitchell et al. [8] studied the detection of antipersonnel landmines by taking thermal images of the soil surface after spraying it with hot water using an array of jets. The variation in conduction and radiation heat transfer due to the water blocked by the mine, and the heating of the mine itself, affected the transient temperature profiles at the soil surface and reflected the presence of the buried mine.

Several numerical studies on thermal signature of buried landmines in dry soil have also been done. Baertlein et al. [15] conducted a study to illustrate the effect of buried landmines on the surface temperature distribution. Khanafer and Vafai [9], using the finite-element method, studied the effect of surface roughness on the thermal signature of mines buried in dry soil over a diurnal cycle. In their study, the insert, which represents the mine's striker mechanism, was accounted for. In another investigation, Khanafer et al. [16] studied the effect of the metal outer case and the top air gap on the soil surface thermal image. However, they neglected the effect of soil moisture on the net heat flux and the governing equations. The work of Van Dam et al. [17] included the effect of moisture content on thermal conductivity and the specific heat of the soil, but did not solve for the moisture distribution in the soil.

From a review of the literature, it is obvious that the effect of soil moisture content on the thermal signature of buried landmines has not been thoroughly investigated, which is essential in delineating the validity and limitation of IR technology for mine detection. In addition, none of the numerical investigations conducted followed the finite-volume approach. To this end, the objective of this article is to present the results of a numerical investigation conducted, using the finite-volume-based model for energy and moisture transfer in soil developed in a companion article [1], to study the effect of moisture content on heat transfer in soil in the presence of a buried landmine. The results obtained are employed to determine the maximum temperature difference between the surface above the mine and the adjacent soil for different types of soils and mines and the times of its occurrence. This, in turn, will help to decide on the best time of day for detecting landmines using IR technology.

It should be mentioned here that this study represents the first step toward the future development of an engineering device capable of detecting landmines in a safe, cheap, and fast manner. The ultimate goal is to develop a hovering machine equipped with an IR camera and other sensors that can fly over a field, take images, and transmit them instantly to a computer for analysis. These images will be compared to others from a database produced by computer simulations to identify existence and location of landmines. As such, accounting for the soil moisture content is important for generating reliable images numerically. However, other factors, not accounted for here, may affect the signature of landmines. For example, vegetation or any other clutter (such as pebbles in the soil) will obscure the signatures and make landmines more difficult to detect. These are not of concern in this work and will be addressed in future studies. Moreover, IR technology is best suited for shallowly buried objects (e.g., antipersonnel mines), as reaffirmed by the results presented in this article.

In the remainder of this article, after a brief description of the physical situation and the equations governing heat and moisture transfer in soil in the presence of a buried landmine, the boundary conditions are introduced. Then an account for the solution procedure is given, followed by results showing the effect of the various parameters involved on the thermal signature of buried landmines.

PHYSICAL MODEL

A schematic of the physical situation and heat exchange processes is depicted in Figure 1a. It consists of a column of soil of depth and diameter both equal to 1 m in which a landmine is buried. The mine is circular in shape, having a diameter of 10 cm and a thickness of 5 cm. The surface of the soil exchanges heat and moisture with the surrounding air and is sunlit from sunrise to sunset. The intention is to study, over a diurnal cycle, the effect of the various parameters (i.e., burial depth, moisture content, time of day, soil type, and landmine type) on the surface thermal signature of the mine, which is buried in the middle of the physical domain. Moreover, the composition of the mine and soil are assumed to be isotropic. With these assumptions, the problem is symmetric with respect to any meridian. Thus, it is sufficient to solve the axisymmetric form of the conservation equations because the solution is independent of the angular position and is a function only of depth and the radial distance from the center of the mine.

GOVERNING EQUATIONS

The conservation equations governing the transfer of moisture and heat in the soil column, using the matric potential-based formulation [1, 18–22] (i.e., ψ – T formulation), are given by

$$C_{\psi\psi} \frac{\partial \psi}{\partial t} + C_{T\psi} \frac{\partial T}{\partial t} = \nabla \cdot (D_{\psi\psi} \nabla \psi) + \nabla \cdot (D_{T\psi} \nabla T) + \frac{\partial K}{\partial z}$$

$$C_{TT} \frac{\partial T}{\partial t} + C_{\psi T} \frac{\partial \psi}{\partial t} = \nabla \cdot (D_{\psi T} \nabla \psi) + \nabla \cdot (k \nabla T) + q'''$$
(1)

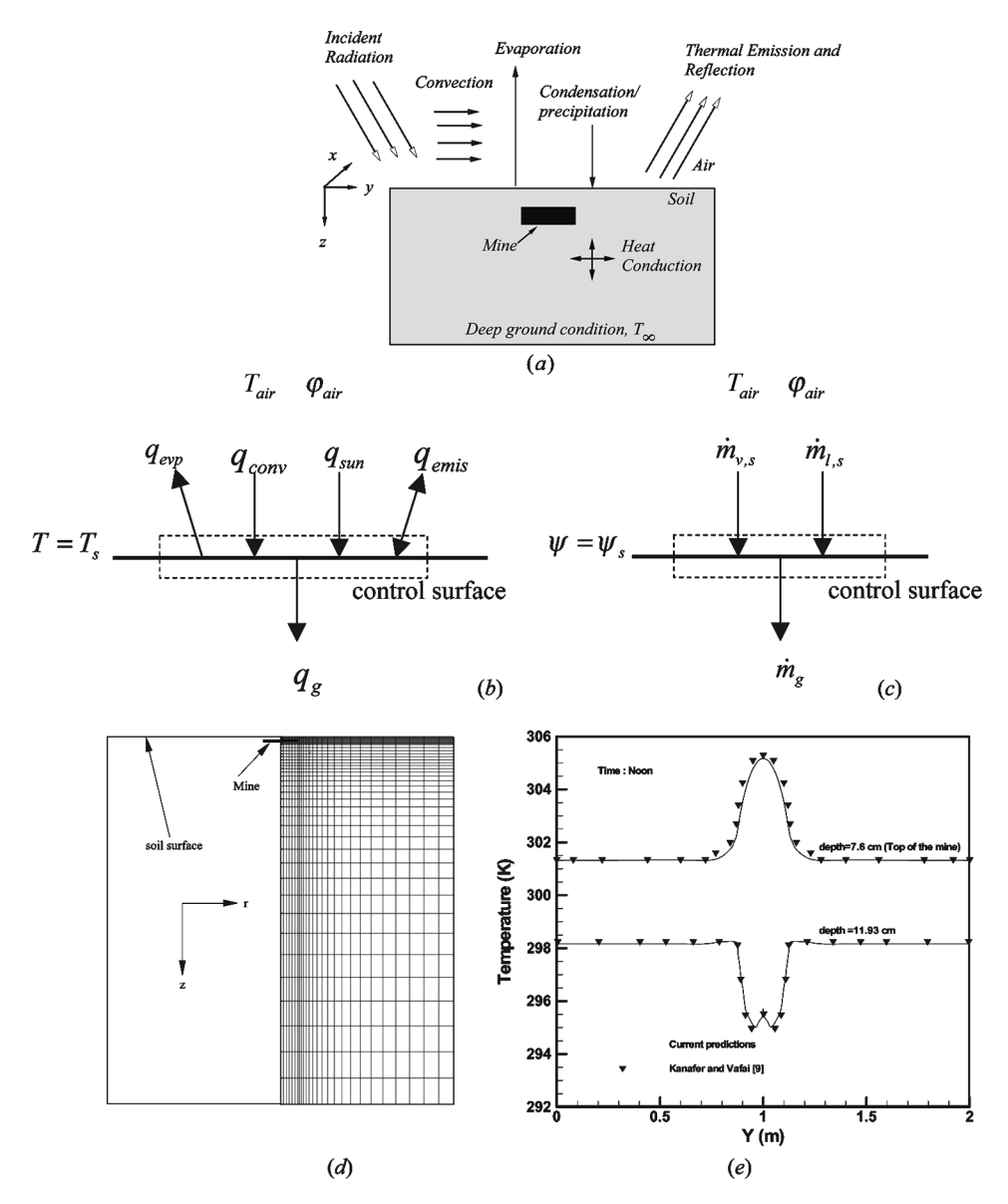


Figure 1. (a) Schematic of the physical situation and heat exchange processes. (b) Moisture balance at the soil surface. (c) Heat balance at the soil surface. (d) An illustrative grid network used. (e) Comparison of predicted soil temperature profiles against those reported in [9].

As stated in [1], the terms of both equations are similar except for the last term on their right side. The terms on the left correspond to the stored mass and energy due to the change in matric potential and temperature. The first two terms on the right side of both equations account for mass and heat transfer, respectively, due to the moisture and temperature gradients. The last term in the first equation represents mass transferred by gravitational effects.

BOUNDARY CONDITIONS

The strongly coupled heat and mass transfer equations [Eq. (1)] require well-defined initial and boundary conditions for predicting the temporal distribution of temperature and moisture in soil. As initial conditions, the uniform distributions of temperature and matric potential in soil are assumed. Converged steady periodic solutions over a diurnal cycle (i.e., 24-h period) that are independent of initial conditions are obtained by iterating in time until the maximum difference in values obtained over two consecutive diurnal cycles is less than a vanishing number ζ , which is set to 10^{-4} .

The most complicated boundary condition is that at the soil surface. In addition, boundary conditions along the vertical sides, the bottom, and the mine-soil interface must also be defined. These are detailed next.

Boundary Condition at the Soil Surface

The soil surface is continuously influenced by atmospheric conditions (Figure 1a), with heat transfer driven by convection, short- and long-wave radiation, as well as latent heat transfer by evaporation and/or condensation. Moisture transfer usually occurs due to evaporation or condensation at the surface and due to moisture addition by rainfall, irrigation, etc.

Surface mass balance. The mass balance at the surface, shown in Figure 1b, requires that the mass flow rate entering and leaving the control surface be equal. Thus,

$$\dot{m}_{v,s} + \dot{m}_{l,s} = \dot{m}_g \tag{2}$$

where $\dot{m}_{v,s}$ is the surface vapor mass transfer due to evaporation or condensation, $\dot{m}_{l,s}$ is the surface liquid transfer due to precipitation, and \dot{m}_g is the moisture transfer into the ground, which takes place in liquid and vapor form and is given by

$$\dot{\mathbf{m}}_g = \rho_l \{ \mathbf{n} \cdot (K \nabla \Phi) + \mathbf{n} \cdot [(D_{\psi\psi} - K) \nabla \psi] + \mathbf{n} \cdot (D_{T\psi} \nabla T) \}$$
 (3)

where the first term on the right-hand side is due to liquid transfer, and the other two terms are due to vapor transfer. Noticing that $\Phi = \psi + z$, the above equation can be rewritten as [1, 21, 22]

$$\dot{m}_g = \rho_I \{ \mathbf{n} \cdot (D_{VVV} \nabla \psi) + \mathbf{n} \cdot (D_{TVV} \nabla T) + \mathbf{n} \cdot [K(\mathbf{k})] \}$$
(4)

The vapor transfer at the surface is due mainly to vapor movement from high-vapor-pressure region to low-vapor-pressure region and is expressed as

$$\dot{m}_{v,s} = \frac{\left(\rho_{v,\text{air}} - \rho_{v,s}\right)}{r_{\text{total}}} \tag{5}$$

where $\rho_{\nu,air}$ and $\rho_{\nu,s}$ are the vapor density at ambient air temperature and soil surface temperature, respectively. The total surface resistance for mass transfer (r_{total}) is equal to the sum of surface (r_s) and aerodynamic (r_a) resistances [23] and is

written as

$$r_{\text{total}} = r_a + r_s \tag{6}$$

The aerodynamic resistance is calculated from

$$r_a = \frac{1}{D_v} \tag{7}$$

where D_v is the vapor diffusion coefficient. Since the heat and mass transfer equations are analogous [24], D_v is usually linked to the thermal diffusion coefficient D_h according to the following relation:

$$D_{\nu} = D_h \left(\frac{D_a}{\alpha_a}\right)^{1-n} \qquad D_h = \frac{h}{\rho_a C_{p,a}} \tag{8}$$

where h, D_a , α_a , ρ_a , and $C_{p,a}$ represent the convective heat transfer coefficient, molecular diffusivity of water vapor in air, thermal diffusivity of air, density of air, and the heat capacity of air, respectively. The exponent n is usually set to 1/3 [24].

Camillo and Gurney [23] found experimentally that the surface resistance behaves as a linear function of the moisture content at the surface (θ_s) , with its value increasing as the soil dries out and approaching zero as the surface moisture reaches a value of 0.2, and suggested the following equation for its calculation:

$$r_s = \max(810 - 4,140\theta_s, 0) \tag{9}$$

The liquid transfer at the surface is due mainly to precipitation or irrigation. Several models [21, 22] have been developed for estimating the moisture flow rate $\dot{m}_{l,s}$ but since no precipitation is considered in this work (i.e., $\dot{m}_{l,s} = 0$), they are not presented. Following the calculation of \dot{m}_g , Eq. (4) is used to evaluate ψ_s at the soil surface.

Surface energy balance. As shown in Figure 1c, energy exchange at the surface occurs via several heat transfer mechanisms, with the heat balance equation written as

$$q_g = q_{\text{conv}} + q_{\text{sun}} + q_{\text{emis}} - q_{\text{evap}} \tag{10}$$

where q_g is the net heat flux through the ground, $q_{\rm conv}$ is the convection heat flux between the surrounding air and the soil surface, $q_{\rm sun}$ is the incident solar energy flux (reduced by cloud cover, atmospheric absorption, albedo, and cosine of the zenith angle), $q_{\rm emis}$ is the long-wave radiation between the soil surface and the sky, and $q_{\rm evap}$ is the heat flux caused by evaporation and/or condensation at the soil surface.

The conduction heat flux through the ground, q_g , is driven by the normal gradients of temperature and matric potential and is given by

$$q_g = \mathbf{n} \cdot [(k\nabla T) + (D_{\Psi T} \nabla \Psi)] \tag{11}$$

The convective heat transfer between the soil surface and the surrounding air is written as

$$q_{\rm conv} = h(T_{\rm air} - T_s) \tag{12}$$

with the ambient temperature at any time, t, computed from

$$T_{\rm air} = T_{\rm avg} - A\cos\left[\frac{2\pi(t-2)}{24}\right] \tag{13}$$

where T_{avg} is the average temperature of the day, A is the amplitude of daily temperature variation from the average, and t is the time of the day in hours on a scale of 1 to 24 starting from midnight. The convective heat transfer coefficient, which depends on the wind speed, u_w , is calculated using the following simple formula from McAdams [25]:

$$h = 5.7 + 3.8u_w \tag{14}$$

Heat transfer by evaporation is evaluated from an equation similar to the one employed for convection and is given by

$$q_{\text{evap}} = h_{fg} D_{\nu} (\rho_{\text{air}} - \rho_{s}) \tag{15}$$

Assuming that the ground surface behaves as a gray body, the long-wave radiation between the soil surface and the atmosphere is expressed as

$$q_{\text{emis}} = \sigma \varepsilon (T_s^4 - T_{\text{sky}}^4) \tag{16}$$

where $\sigma = 5.67 * 10^{-8} \text{ W/m}^2 \text{ K}^4$ is the Stefan-Boltzmann constant, ε is the mean emissivity of the surface, T_s is the soil's surface temperature, and $T_{\rm sky}$ is the effective sky radiant temperature given by

$$T_{\rm sky} = 0.9 \times T_{\rm air} \tag{17}$$

The short-wave incident solar radiation is expressed as

$$q_{\text{sun}} = (1 - C_L)S_o(1 - C)M(\phi)\cos(\phi) \tag{18}$$

where C_L is the cloud cover, C (=0.3) is the ground albedo, and S_o (=1,385 W/m²) is the solar constant. Moreover, $M(\phi)$ is the approximate atmospheric transmissivity given by

$$M(\phi) = 1 - 0.2[\cos(\phi)]^{-0.5}$$
 (19)

In Eq. (19), ϕ is the zenith angle calculated using the following expression:

$$\cos(\phi) = \max\left[0, -\cos(\lambda)\,\cos(\delta)\,\cos\left(\frac{2\pi t}{24}\right) + \sin(\lambda)\,\sin(\delta)\right] \tag{20}$$

where λ is the local latitude and δ is the declination angle computed from

$$\delta = -23.43^{\circ} \cos(2\pi \operatorname{month}/12) \tag{21}$$

The various terms in Eq. (10) are substituted for by their equivalent expressions and the resulting equation is used to calculate the temperature at the soil surface (T_s) .

Other Boundary Conditions

In addition to the boundary conditions at the surface of the soil, boundary conditions at the vertical sides of the domain are also needed. The normal fluxes along the centerline and outer vertical boundary of the axisymmetric domain are set to zero (Figure 1*d*). Mathematically this is equivalent to

$$\left\{ \begin{array}{l} \mathbf{n} \cdot (D_{\psi\psi} \nabla \psi + D_{T\psi} \nabla T) = 0 \\ \mathbf{n} \cdot (k \nabla T + D_{\psi T} \nabla \psi) = 0 \end{array} \right\} \Rightarrow \mathbf{n} \cdot \nabla \psi = \mathbf{n} \cdot \nabla T = 0 \tag{22}$$

Moreover, the mine is treated as a homogeneous solid object having the same thermal properties as the explosives of which it is composed (e.g., TNT) and of zero moisture content. The presence of the mine in the calculation domain is accounted for by the special treatment suggested by Patankar [26]. The mine–soil interface is assumed impermeable for flow of moisture and the normal gradient of the matric potential is therefore set to zero (i.e., $\mathbf{n} \cdot \nabla \psi = 0$). Additionally, conservation of energy requires a continuous heat flux across the mine–soil interface. Then the equation to be satisfied is given by

$$(\mathbf{n} \cdot k \nabla T)_{\text{soil}} = (\mathbf{n} \cdot k \nabla T)_{\text{mine}} \tag{23}$$

Because a conservative scheme is used, arranging the control-volume face to coincide with the mine interface ensures energy balance at the mine–soil interface and forces Eq. (23) to be implicitly satisfied. Finally, at the bottom boundary of the domain, which is taken deep enough not to influence the solution, T and ψ are both assigned constant values.

SOLUTION PROCEDURE AND NUMERICAL ACCURACY

The coupled system of heat and moisture equations [Eq. (1)] subject to the above-described initial and boundary conditions is solved numerically using the control-volume method that was detailed in a companion article [1]. In this procedure, the solution domain is subdivided into a number of control volumes, each associated with a grid point located at its geometric center. By first integrating the equations over each control volume and then using Green's theorem to replace the volume integral with the surface integral, we obtain the discretized forms. With suitable profile interpolation in each coordinate direction for the variables whose values are unknown on the control-volume faces, a system of algebraic equations results

that can be solved iteratively using a line-by-line Thomas algorithm [26]. Moreover, grid networks, illustrated in Figure 1d, are generated using the transfinite interpolation technique [27].

The credibility of the numerical method was established in [1] by presenting results validating the implementation of the various terms involved in the conservation equations. To verify the correct implementation of the boundary conditions at the surface of the soil, the results reported by Khanafer and Vafai [9] using a finite-element approach for a buried landmine in dry soil are reproduced and comparison of temperature profiles at two depths of 0.076 and 0.1193 m are displayed in Figure 1e. As depicted, current predictions are in good agreement with published results. The slight difference in values is attributed to some error introduced while extracting data from small figures and to the different mesh and time step used. A fixed time step of 30 s is used in this work, while Khanafer and Vafai [9] used a variable time step with a minimum value of 0.36 s.

RESULTS AND DISCUSSION

As described above, the physical configuration of interest involves a circular antipersonnel landmine, 10 cm in diameter and 5 cm in thickness, buried in a cylindrical container of diameter 1 m filled with soil to a height of 1 m. Results are generated in dry and moist soils for different uniform initial values of moisture content and the effects of varying the burial depth, soil type, and mine type on the thermal signature of the landmine are analyzed. The average air temperature is set at 28°C with amplitude of 4°C. This represents a typical day in July in a country like Lebanon, and the relative humidity is held constant at 80%. The duration of each run is 240 h (10 days), which is found to be sufficient to reach a periodic converged solution over a diurnal cycle.

To investigate the sensitivity of the solution to the time step and grid used, numerical experiments are carried out with different time steps and nonuniform grid networks, for both dry and moist soils. For dry soil an initial temperature of 293 K is used, whereas for moist soil the initial temperature and matric potential are set at 293 K and -10 m, respectively. In both cases, the landmine is buried at a depth of 2 cm. The results are generated for three different time steps with values of 30, 120, and 180 s, and three different nonuniform grid networks of sizes, 30×21 , 40×28 , and 50×35 control volumes. When varying the time step, a grid of size 40×28 control volumes is used, and when varying the grid size, a time step of value 120 s is employed. A plot illustrating the grid utilized in the computations is displayed in Figure 1d.

Surface profiles for different grid sizes and time steps at three different times of the day are depicted in Figure 2. Results in Figures 2a and 2b are for moist soil, while those in Figures 2c and 2d are for dry soil. Figure 2a presents surface profiles of moisture content, whereas Figures 2b-2d display surface profiles of temperature. Profiles in Figures 2a and 2c are generated using different grid networks, while those in Figures 2b and 2d are predicted employing various time steps. As shown, profiles are almost indistinguishable, showing a time-step- and grid-independent solution, for both moist and dry soils. As a compromise between cost and accuracy, all results presented in this work are generated using a time-step value of $120 \, \text{s}$ over a nonuniform

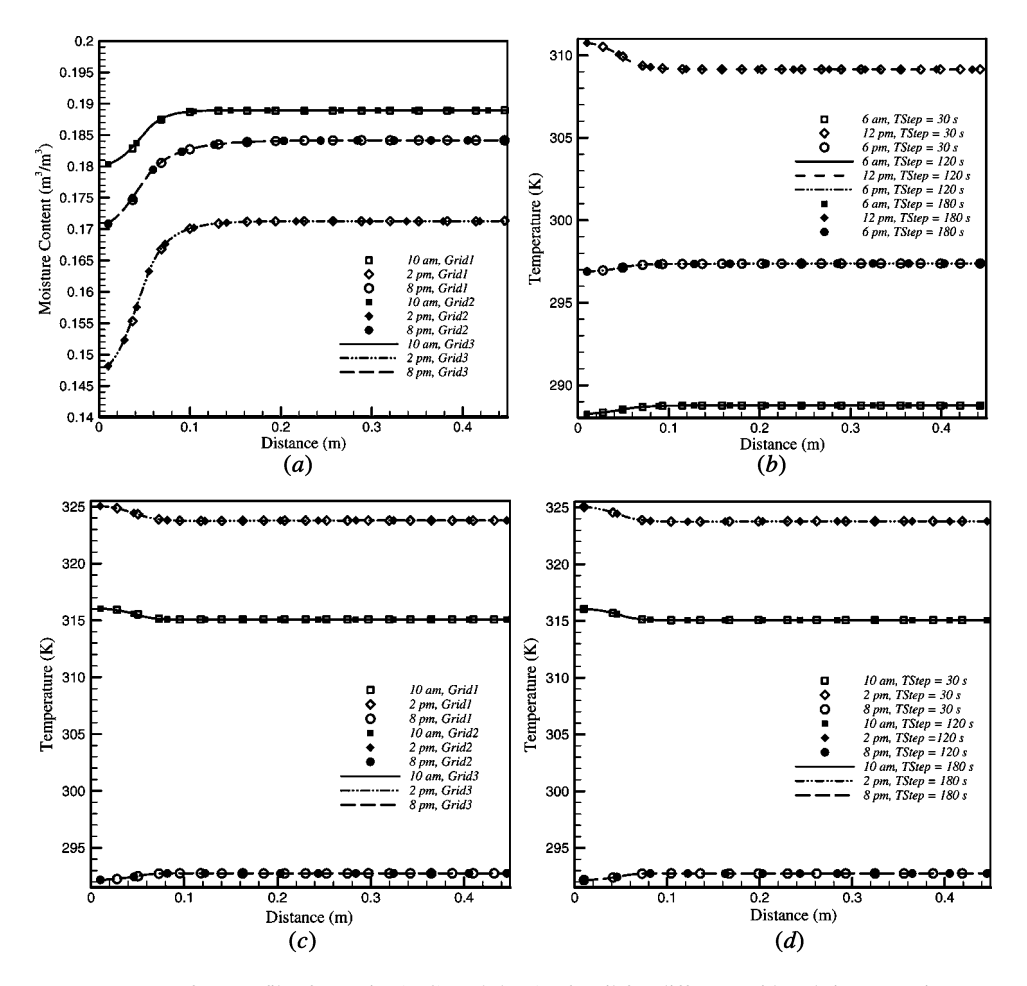


Figure 2. Surface profiles for moist (a, b) and dry (c, d) soil for different grid and time-step sizes.

mesh of size 40×28 control volumes. Grid points are clustered close to the surface and solid boundaries, where large gradients are expected (Figure 1*d*).

Effects of Different Parameters

To investigate the effects of mine and soil type, burial depth, and moisture content on heat and mass transfer in soils and to assess their impact on the thermal contrast at the soil surface, computations are performed for several burial depths and soil moisture contents using two landmine types (TNT and Tetryl) and three soil types (Yolo light clay, sandy clay loam, and heavy clay), whose physical properties are given in Appendix I.

Effect of mine material and burial depth. To examine the effect of burial depth on the thermal contrast at the soil surface and to identify the maximum depth after which no thermal signature appears at the soil surface, computations are

performed using two landmine types (TNT and Tetryl) buried in dry and moist heavy clay soil at various depths (1, 2, 4, 6, and 8 cm); results are displayed in Figures 3–8.

The temperature distributions at the surface of dry and moist soil $(\psi_i = -10 \,\mathrm{m})$, in which a landmine of type TNT is buried at various depths, are presented at different times of the day in Figures 3 and 4, respectively. Profiles clearly indicate that, for both dry and moist soil, increasing the burial depth decreases the thermal contrast until it nearly vanishes at a burial depth of 8 cm. The thermal conductivity of TNT being lower than that of soil (i.e., $k_{\mathrm{TNT}} = 0.22 \,\mathrm{W/m}\,\mathrm{K}$), increases the thermal resistance to heat transfer (thermal resistance is inversely proportional to thermal conductivity) along the portion of the path containing the mine. Therefore heat transferred through the soil above the mine faces higher thermal resistance with a consequent increase in temperature there during the heating period (Figures 3b, 3c,

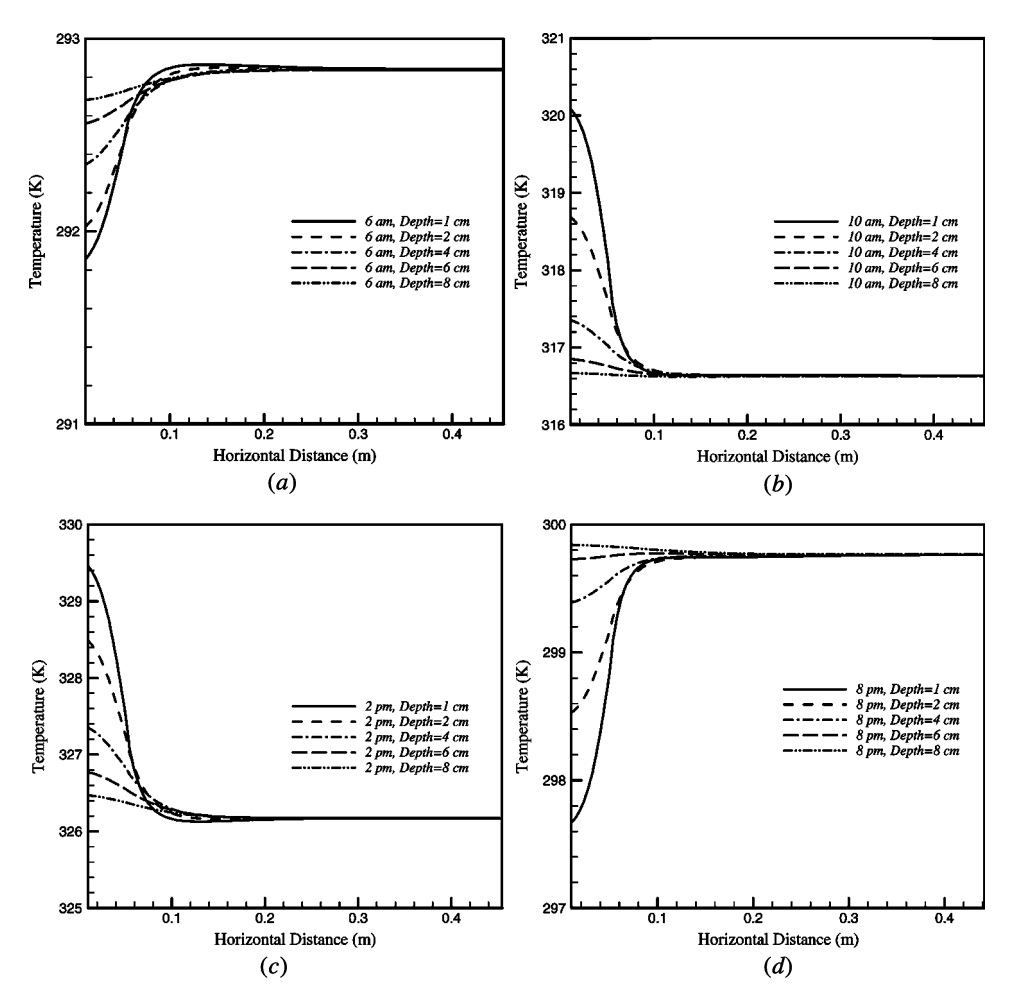


Figure 3. Effect of TNT mine's burial depth on surface temperature distribution of dry heavy clay soil at (a) 6 a.m., (b) 10 a.m., (c) 2 p.m., and (d) 8 p.m.

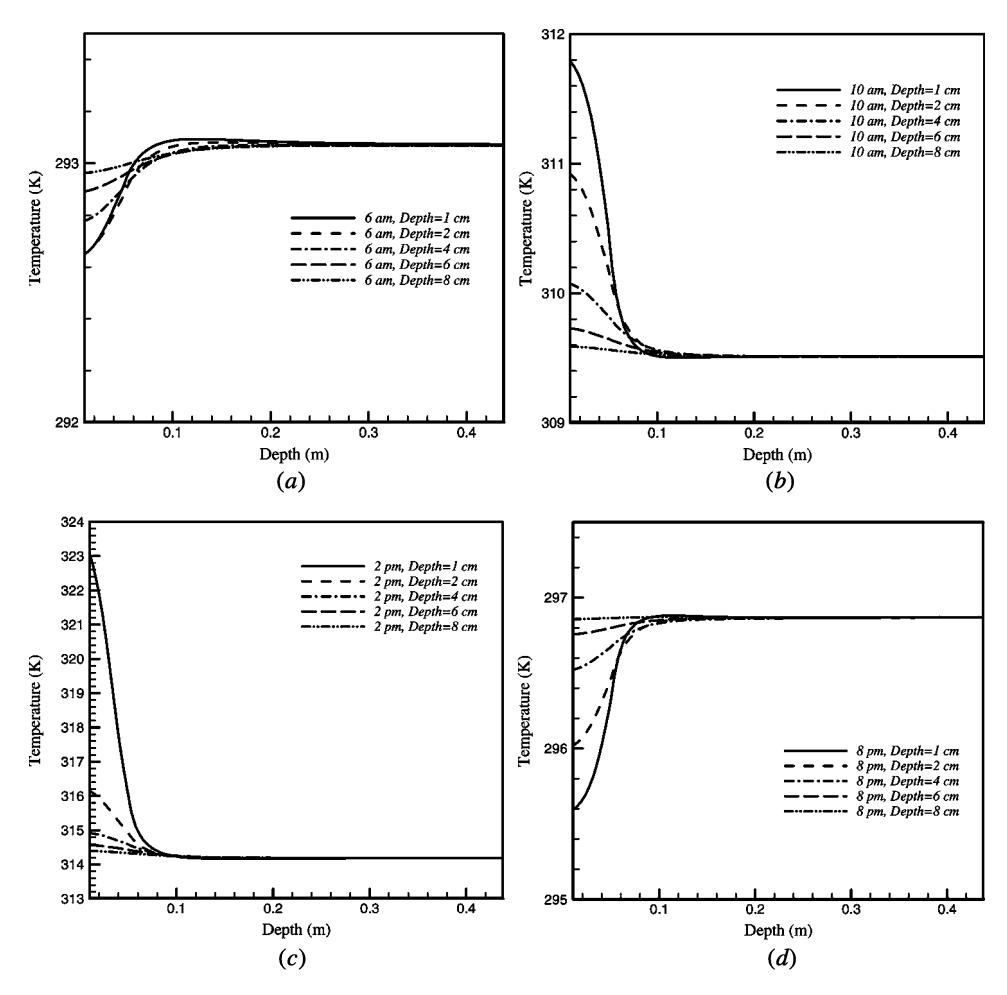


Figure 4. Effect of TNT mine's burial depth on surface temperature distribution of moist heavy clay soil $(\psi_i = -10 \text{ m})$ at (a) 6 a.m., (b) 10 a.m., (c) 2 p.m., and (d) 8 p.m.

4b, and 4c), leading to a visible thermal contrast at the surface. The maximum value of this thermal contrast depends on the type and moisture content of the soil. During the cooling phase (Figures 3a, 3d, 4a, and 4d), the hot part above the mine becomes cooler than the surrounding soil due to the tendency of the mine to block the upward heat transfer by conduction through the soil, which results in a thermal contrast having a sign opposite to that obtained during heating.

The soil temperature profiles at three different depths are depicted for dry and moist heavy clay soil in Figures 5 and 6, respectively. Results are presented for a configuration in which the upper surface of the buried mine is 1 cm below the soil surface. The selected depths coincide with the soil surface, the mid-height of the mine (i.e., at a depth of 3.5 cm), and a location 1 cm below the lower surface of the mine (i.e., at a depth of 7 cm). The surface temperature definitely reveals the signature of the landmine, and the inclusion of internal soil temperature profiles serves as a check

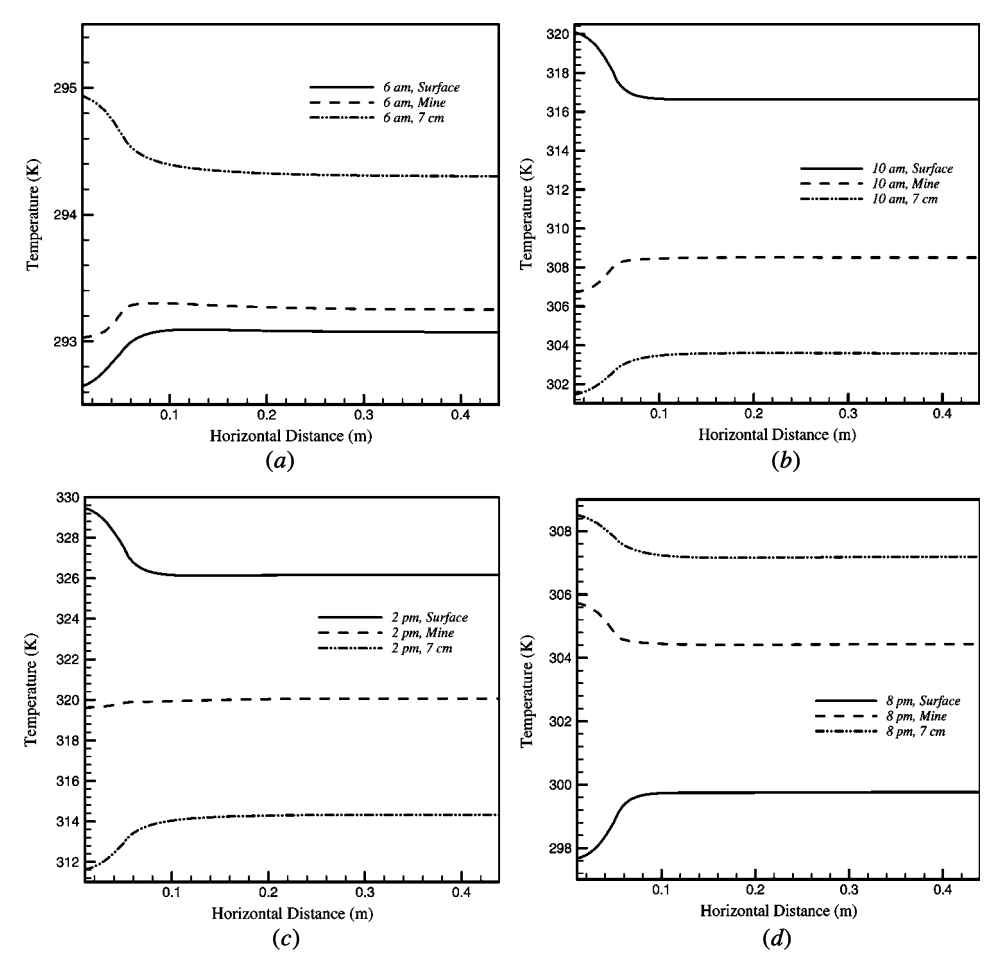


Figure 5. Temperature distribution for dry heavy clay at different depths and times using TNT buried mine at a depth of 1 cm.

of the validity of results, i.e., they help in identifying any unphysical behavior. Predictions displayed at four different times of the day (6 a.m., 10 a.m., 2 p.m., and 8 p.m.) show the effect of the presence of the mine on conduction heat transfer in the soil. In the early morning (Figures 5a and 6a), the soil surface temperature is lower than the temperature of the soil below the surface. As heating by solar radiation continues, the picture is reversed (Figures 5b, 5c, 6b, 6c). Then, after sunset, cooling starts and the soil surface temperature is again lower (Figures 5d and 6d). However, the temperature of the soil above the mine as compared to the temperature of the soil surrounding the mine does not follow the same trend. At 6a.m. (Figures 5a and 6a), the soil temperature below the mine is higher than the temperature of the soil away from the mine at the same depth. This is due to the fact that the mine acts as a barrier or an insulator, reducing heat transfer. For the same reason, the temperatures of the mine and the soil above the mine are lower than their surrounding

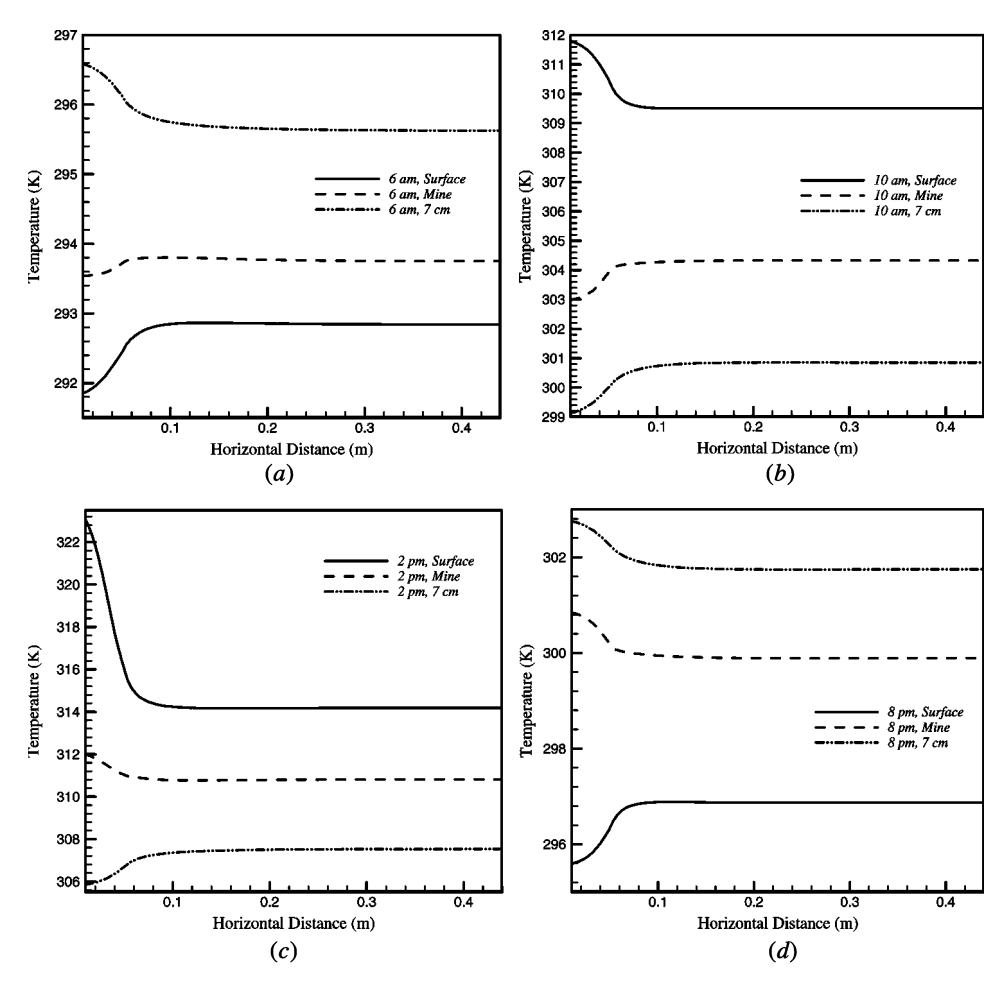


Figure 6. Temperature distribution for moist heavy clay ($\psi_i = -10 \,\mathrm{m}$) at different depths and times using TNT buried mine at a depth of 1 cm.

soil. As time progresses, the soil starts to be heated by short-wave solar radiation. By 10 a.m. (Figures 5b and 6b), the soil at the surface becomes hotter than the soil deep below and the soil temperature decreases with depth. However, the insulating effect of the mine causes the soil surrounding the mine to become hotter than the mine. After a sufficient heating time (i.e., at 2 p.m., Figures 5c and 6c), the mine temperature increases and becomes very close to the temperature of the surrounding soil for the dry case (Figure 5c) and higher than the surrounding soil for the moist case (Figure 6c). In moist soil, this behavior is due to the evaporation, which is greater over the mine than away from it because of the heat trapped there. As cooling takes place (Figures 5d and 6d), the insulating effects of the mine reduce the rate at which heat flows upward through it and cause the temperature above the mine to be higher than the temperature of the surrounding soil.

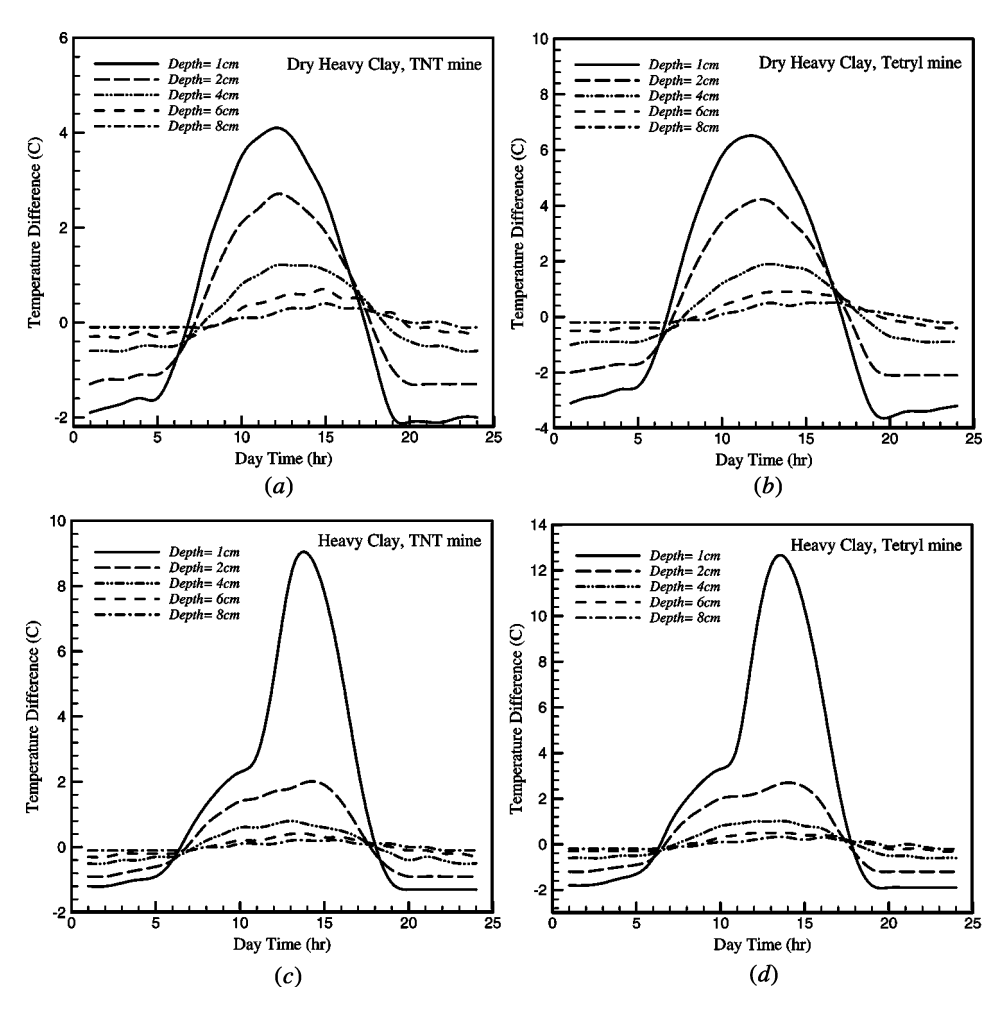


Figure 7. Thermal contrast at the surface for different burial depths over a diurnal cycle for (a) dry heavy clay using TNT mine, (b) dry heavy clay using Tetryl mine, (c) moist heavy clay ($\psi_i = -10 \,\mathrm{m}$) using TNT mine, and (d) moist heavy clay ($\psi_i = -10 \,\mathrm{m}$) using Tetryl mine.

The thermal contrast is defined in this work as the temperature difference between the point on the soil surface above the mine center and a reference point at the surface where no mine is buried. The thermal contrasts at the surface over a diurnal cycle for different burial depths of two types of landmine are presented in Figures 7 and 8 for dry and moist heavy clay soil, respectively. Figure 7 clearly shows that for both dry and moist soil, the burial depth has influence on the time of occurrence of the maximum thermal contrast at the surface and on the maximum contrast amplitude. The maximum thermal contrast decreases as the mine burial depth increases, and its maximum shifts during the heating phase toward later hours in the day. The time shift is due to the higher storage capacity of the soil above the mine, causing a slower thermal response to heating. The presence of moisture has a

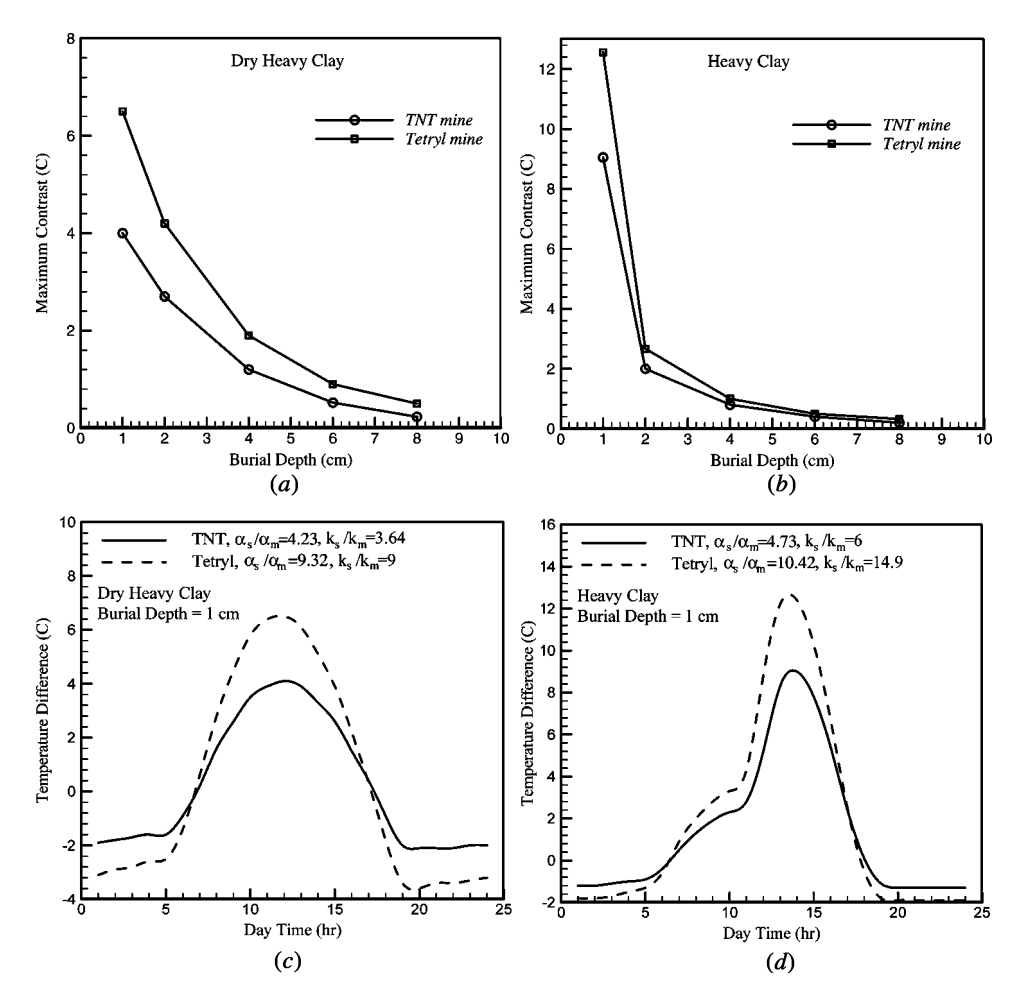


Figure 8. Maximum thermal contrast at the surface using TNT and Tetryl mines for (a) dry heavy clay versus burial depth, (b) moist heavy clay ($\psi_i = -10 \,\mathrm{m}$) versus burial depth, (c) dry heavy clay versus time of the day for 1-cm burial depth, (d) moist heavy clay ($\psi_i = -10 \,\mathrm{m}$) versus time of the day for 1-cm burial depth.

more pronounced effect on shifting the time of occurrence of the maximum contrast, where, for a mine buried at a depth of 1 cm, the dry soil maximum contrast takes place at noon, while for wet soil it happens at 2 p.m. Increasing the mine thermal resistance has significant effect on the thermal contrast, where a temperature difference of 6.3° C is attained on the soil surface for Tetryl mine buried at 1 cm depth in dry heavy clay (see Figure 7b), compared to 4° C attained for a TNT mine buried at the same depth and in the same type of soil (see Figure 7a). However, the presence of moisture in the soil greatly influences the magnitude of the maximum thermal contrast and the time of the day when the maximum contrast occurs. By comparing plots in Figure 7 (i.e., Figure 7a against Figure 7b and Figure 7c against Figure 7d),

it is clear that at low burial depths (less than 1 cm here), the thermal contrast is higher in moist soil than in dry soil. The maximum thermal contrast for a TNT mine buried at a depth of 1 cm increases from 4°C for dry heavy clay soil (Figure 7a) to 9.23°C for moist heavy clay soil at $\psi_i = -10 \,\mathrm{m}$, and the time of day when the maximum contrast occurs in that case shifts from noon for dry soil to 2 p.m. for moist soil. Similar behavior is observed in Figures 7b and 7d for a Tetryl mine buried in dry and moist soils. However, as the burial depth increases, the magnifying effects of the soil moisture content disappear. This is further revealed in Figures 8a and 8b, which present the variation of maximum contrast at the soil surface with burial depth. As shown, there is a sharp decrease in the maximum contrast with an increase in the burial depth from 1 to 2 cm. This is not the case with dry soil, where the maximum contrast decreases smoothly with depth. The evaporation taking place in moist soil is the main reason for this behavior. At a burial depth of 1 cm, the moisture at the surface above the mine rapidly evaporates, leading to a big difference in thermal conductivity between it and the surrounding soil with no possibility for axial moisture diffusion due to the presence of the mine. This difference results in a high thermal contrast. As the burial depth increases, the rate of decrease of moisture content above the mine decreases, leading to lower thermal contrast. Furthermore, the effects of mine type on the thermal signature, for both dry and moist soil, are depicted in Figures 8c and 8d, respectively. As the thermal diffusivity and conductivity of the mine decreases, the maximum contrast increases. For the case presented, as the thermal diffusivity ratio $\alpha_{\text{soil}}/\alpha_{\text{mine}}$ increases from 4.23 to 9.32 for dry soil and from 4.73 to 10.42 for moist soil, the thermal contrast increases by 2.3 and 3.4°C, respectively.

Effect of water content and soil type. The simultaneous temperature and moisture changes in soil, induced by variations in surface moisture and heat fluxes, are highly dependent on the type of soil and its physical properties. The three types of soil selected in this study are heavy clay (70% clay, 20% sand, and 10% silt), sandy clay loam (28% clay, 56% sand, and 16% silt), and Yolo light clay (31.2% clay, 23.8% sand, and 45% silt). The variation of soil material properties (moisture retention, thermal conductivity, thermal capacity, and hydraulic conductivity) with moisture content is most pronounced when the sand content is high, while silt or clay has less influence [28].

The effect of initial moisture content and soil type on the surface thermal signature of buried landmines is investigated by generating numerical solutions of heat and moisture diffusion in the three mentioned types of soil using four different initial distributions of the soil matric potential of values -1, -10, -100, and -500 m. As the thermal contrast decreases with increasing burial depth, all results presented in this section (Figures 9–12) are obtained for a mine buried at 1 cm below the soil surface in order to demonstrate clearly the effects of the above-mentioned parameters.

Surface temperature and matric potential profiles for different initial moisture contents at two times of the day (6 a.m. and 2 p.m.) using a TNT buried mine are presented for the heavy clay, sandy clay loam, and Yolo light clay soil in Figures 9, 10, and 11, respectively. As the variation of temperature with time for a given matric potential was discussed in the previous section, discussion will concentrate here on the effects of the moisture content and soil type. Figures 9–11 show the radial variation

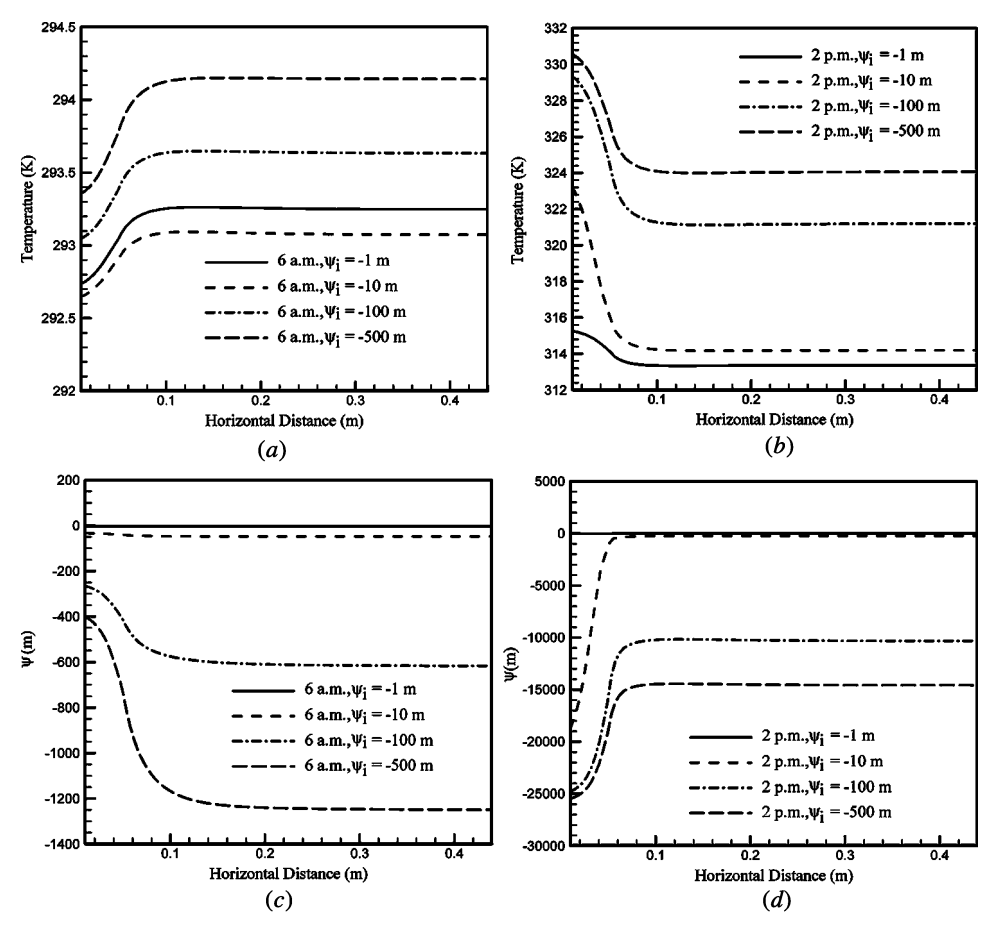


Figure 9. Surface temperature and matric potential distribution for heavy clay, for different matric potentials and different times using TNT buried mine at a depth of 1 cm.

of surface temperature profiles at 6 a.m. (Figures 9a-11a) and 2 p.m. (Figures 9b-11b), and the corresponding radial matric potential profiles in Figures 9c-11c and Figures 9d-11d, respectively. With the exception of the temperature profile of heavy clay soil for $\psi_i = -10$ m at 6 a.m. (Figure 9a), the surface temperature increases with decreasing moisture content (or matric potential). This is expected because the higher the wetness of the soil is, the more heat will be required for evaporation. Consequently, less heat will be available to sensibly heat the soil and increase its temperature. For the profile in Figure 9a ($\psi_i = -10$ m), the temperature is seen to be lower than the corresponding profile for $\psi_i = -1$ m. This behavior is attributed to the competing effects of the soil thermal conductivity and specific heat, which both increase with increasing moisture content as the trapped air in the pores is replaced by water. Therefore the thermal diffusivity of the soil, which is the ratio of thermal conductivity to volumetric heat capacity, depends heavily on the moisture content of the soil. Moreover, thermal diffusivity is the controlling transport property for transient

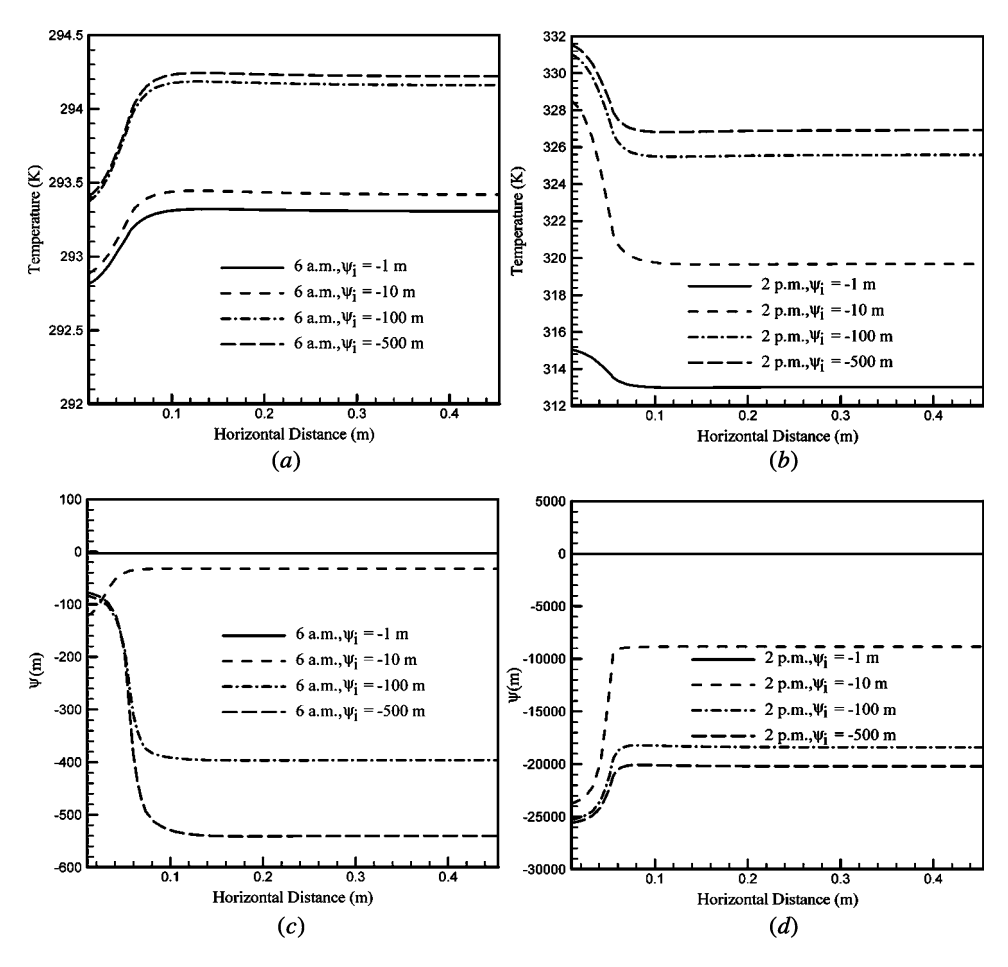


Figure 10. Surface temperature and matric potential distribution for sandy clay loam soil, for different matric potentials and different times using TNT buried mine at a depth of 1 cm.

conduction heat transfer that determines the rate at which the soil responds to environmental changes [24]. As shown in the legend of Figure 12a, for heavy clay soil the soil-to-mine thermal diffusivity ratio changes from $\alpha_s/\alpha_m=4.73$ at $\psi_i=-1$ m to $\alpha_s/\alpha_m=4.71$ at $\psi_i=-10$ m, while the corresponding thermal conductivity ratio changes from $k_s/k_m=6$ to $k_s/k_m=4.9$. Therefore it is possible for the thermal diffusivity at two different matric potential values to be nearly equal while the thermal conductivities are quite different, and explains the higher temperature obtained at a higher matric potential value.

In general, the matric potential profiles vary in an opposite manner to the temperature profiles. Results reveal that at 6 a.m. (Figures 9c-11c) the moisture content of the soil above the mine is higher than the surroundings, while at 2 p.m. (Figures 9d-11d) it is lower (i.e., drying of the soil is faster above the mine). These results clearly show that at a given depth the water content can either decrease or increase away from the mine due to the blocking effect the mine creates prohibiting any

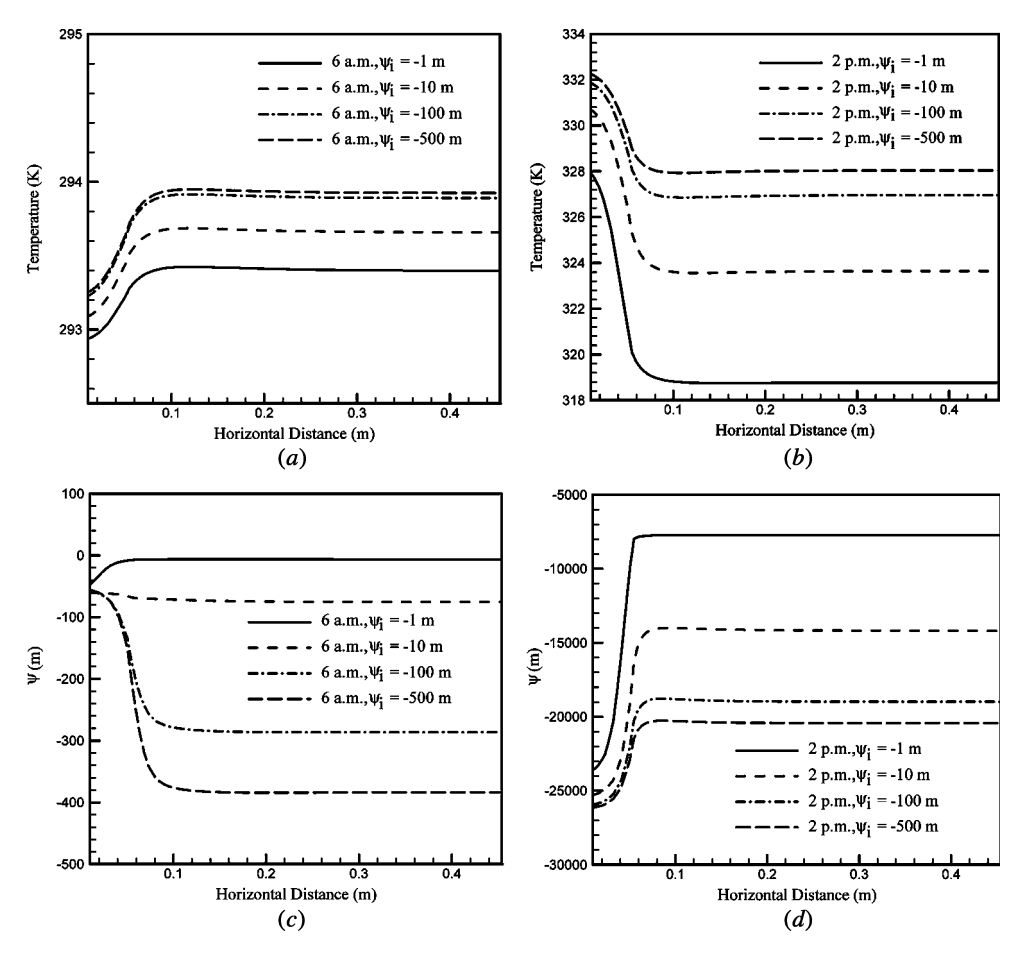


Figure 11. Surface temperature distribution and matric potential for Yolo light clay, for different matric potentials and different times using TNT buried mine at a depth of 1 cm.

transfer of moisture in the axial direction. The exception is for sandy clay loam at $\psi_i = -10 \,\mathrm{m}$ and Yolo light clay at $\psi_i = -1 \,\mathrm{m}$, which vary in the same direction as temperature. This is a clear indication that the landmine affects soil water content distributions around it in a very dynamic way depending on the influence of soil thermal and hydraulic properties on moisture diffusion as explained earlier.

The variation of surface thermal contrast over a diurnal cycle for different initial moisture content are presented in Figures 12a-12c for heavy clay, sandy clay loam, and Yolo light clay soil, respectively, using a TNT mine buried at a depth of 1 cm. The variations of the maximum thermal contrast with initial moisture content for the three types of soil are depicted in Figure 12d. For the types of soil used, the soil-to-mine thermal diffusivity ratio α_s/α_m increases by 10–11% and the soil-to-mine thermal conductivity ratio k_s/k_m increases by 65–80% when the matric potential ψ_i in the soil is increased from –500 m to –1 m. The changes in soil thermal properties cause a phase shift in the time of the day when maximum thermal contrast occurs.

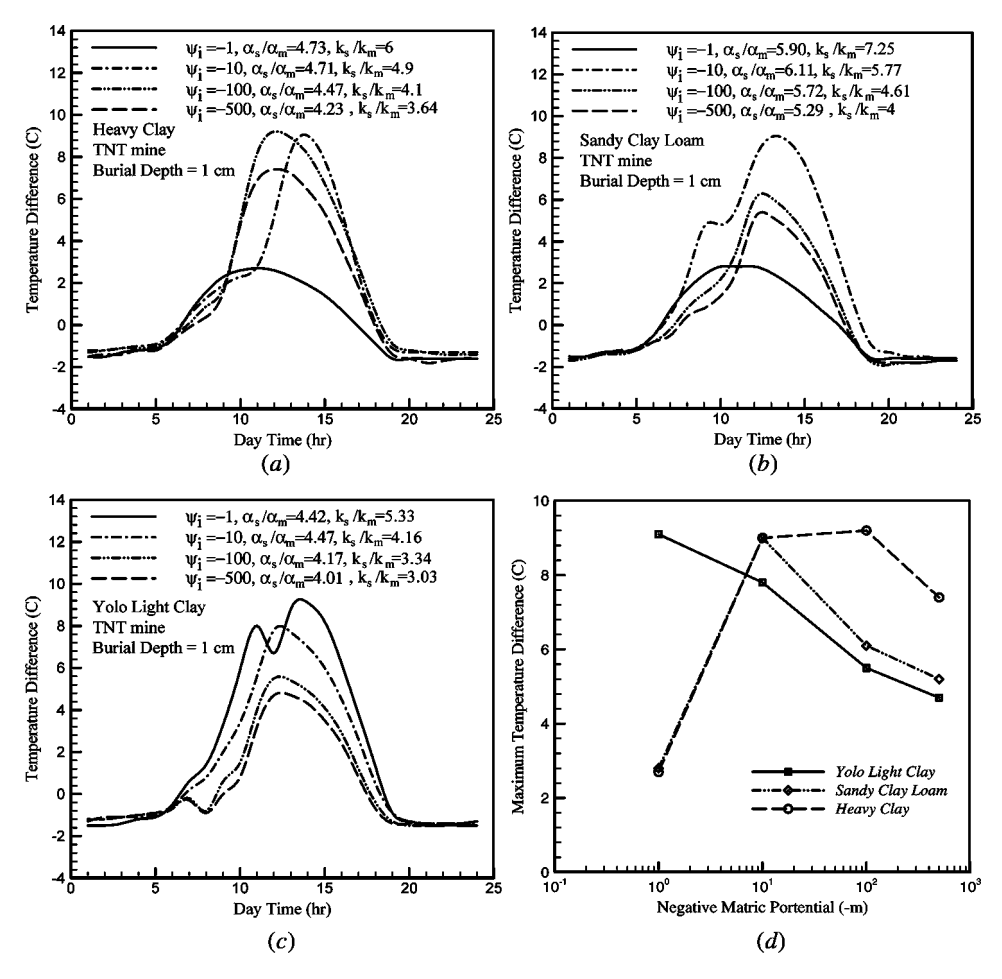


Figure 12. Variation of surface thermal contrast over a diurnal cycle at different initial moisture contents for (a) heavy clay, (b) sandy clay loam, (c) Yolo light clay soil using TNT mine buried at 1-cm depth, and (d) maximum thermal contrast variation with initial moisture content for three types of soil.

The time of peak contrast of heavy clay soil, for example, occurs at 12:00 noon, 12:00 noon, 2:00 p.m., and 10:30 a.m. for $\psi_i = -500$, -100, -10, and -1 m, respectively. Heavy clay soil has low hydraulic conductivity, enabling it to retain moisture close to the soil–air interface. At high moisture content of $\psi_i = -1$ m, the heavy clay maximum thermal contrast (2.5°C) is smaller than the contrast (9.3°C) observed for lower moisture content ($\psi_i = -100$ m), indicating that a change of phase is taking place by evaporation that results in less sensible heating of the soil. Sandy clay loam shows similar behavior as heavy clay, where the maximum thermal contrast of 9°C is attained at $\psi_i = -10$ m. The thermal contrast shown in Figure 12c increases as the initial soil moisture content is increased.

The initial matric potential values that maximize the thermal contrast are -1,-10, and -100 m for Yolo light clay, sandy clay loam, and heavy clay soil, respectively (see Figure 12*d*). This can be explained by the fact that, as moisture content

increases in the soil, the trapped air in the pores is replaced with water, which leads to an increase in both the thermal conductivity and volumetric heat capacity of the soil. The three types of soil exhibit smaller thermal contrast during cooling (at night) compared to heating, with the difference in temperature being smaller than 2°C due to absorption of moisture from air.

CLOSING REMARKS

A finite-volume numerical method was used for studying the effect of soil type, soil moisture content, mine type, and mine burial depth on the thermal signatures of buried landmines. Results indicated that as the burial depth of the mine increases, the thermal contrast at the soil surface becomes weaker. The addition of moisture was found to enhance the thermal contrast at a burial depth of 1 cm in heavy clay soil. However, enhancement of the thermal signature was found to be limited to shallowly buried mines (up to 2 cm), as moisture evaporation takes place at the surface. The type of soil was found to have a profound influence on the thermal signature, with high moisture content in heavy clay soil resulting in degraded thermal contrast because of the change of phase that takes place during drying. Moreover, increasing the moisture content in the soil shifted the time of the day at which the maximum thermal contrast occurred. Moreover, the prediction of mine thermal signatures on soil surface was found to rely on accurate determination of soil parameters including soil matric potential and thermal conductivity. These parameters do not have fixed relationships with each other but depend on soil properties and textures, which further complicate their expected thermal response.

REFERENCES

- 1. F. Moukalled and Y. Saleh, Heat and Mass Transfer in Moist Soil, Part I. Formulation and Testing, *Numer. Heat Transfer B*, vol. 49, pp. 467–486, 2006.
- J. R. Simard, Improved Landmine Detection Capability (ILDC): Systematic Approach to the Detection of Buried Mines Using Passive IR Imaging, in A. C. Dubey, R. L. Barnard, C. J. Lowe, and J. E. McFee (eds.), *Detection and Remediation Technologies for Mines and Mine-like Targets, Proc. SPIE*, Orlando, FL, vol. 2765, April 9–12, pp. 489–500, 1996.
- 3. P. D. Gader, M. Mystkowski, and Y. Zhao, Landmine Detection with Ground Penetrating Radar Using Hidden Markov Models, *IEEE Trans. Geosci. Remote Sensing*, vol. 39, no. 6, pp. 1231–1244, 2001.
- 4. J. M. Phelan and S. W. Webb, Environmental Fate and Transport of Chemical Signatures from Buried Landmines: Screening Model Formulation and Initial Simulations, Sandia National Laboratories Report SAND97-1426, Albuquerque, NM, June 1997.
- 5. A. Hudson, A. Chongpison, D. Loganathan, and J. Kury, The Quadrupole Resonance Properties of Nondetonable Explosive Formulations for Landmine Detection Machine Calibration and Testing, *Appl. Magnet. Resonance*, vol. 25, pp. 355–370, 2004.
- 6. F. Moukalled, N. Ghaddar, H. Kabbani, N. Khaled, and Z. Fawaz, Numerical and Experimental Investigation of Thermal Signatures of Buried Landmines in Dry Soil, *Proc.* 2005 ASME Summer Heat Transfer Conf., San Francisco, CA, July 17–22, 2005.
- 7. Y. H. Janssen, A. N. Jong, H. Winkel, and F. J. Putten, Detection of Surface-Laid and Buried Mines with IR and CCD Cameras: An Evaluation Based on Measurements, in Detection and Remediation Technologies for Mines and Mine-like Targets, in A. C. Dubey,

- R. L. Barnard, C. J. Lowe, and J. E. McFee (eds.), *Proc. SPIE*, vol. 2765, pp. 448–459, April 1996.
- 8. R. Mitchell, S. Somu, and S. Agarwal, Detection of Antipersonnel Landmines Based on Water Jet-Induced Thermal Images, *Proc. SPIE—Int. Soc. Opt. Eng.*, vol. 3710, no. 1, pp. 180–188, 1999.
- 9. K. Khanafer and K. Vafai, Thermal Analysis of Buried Land Mines over a Diurnal Cycle, *IEEE Trans. Geosci. Remote Sensing*, vol. 40, no. 2, pp. 461–473, 2002.
- 10. M. Larive, D. Spoliansky, and O. Trezieres, Pre-processing of 8–12 µm Polarimetric Features for Laid and Flush-Buried Mines Detection, *Proc. SPIE—Int. Soc. Opt. Eng.*, vol. 3710, no. 1, pp. 197–202, 1999.
- 11. A. Filippidis, L. C. Jain, and P. Lozo, Degree of Familiarity ART2 in Knowledge-Based Landmine Detection, *IEEE Trans. Neural Networks*, vol. 10, pp. 186–192, 1999.
- 12. C. Bruschini and B. Gros, A Survey of Current Sensor Technology Research for the Q7 Detection of Landmines, in Sustainable Humanitarian Demining: Trends, Technologies and Technologies, edited by the Humanitarian Demining Information Center, James Madison University (Co-Editors: D. Barlow, C. Bowness, A. Craib, G. Gately, J.-D. Nicoud, J. Trevelyan), Mid Valley Press, Verona, VA, USA, pp. 172–187, December 1998.
- 13. J. Deans, G. Schmithals, and L. J. Carter, An Analysis of a Thermal Imaging Method for Landmine Detection Using Microwave Heating, *J. Appl. Geophys.*, vol. 47, no. 2, pp.123–133, 2001.
- 14. J. Hermann and I. Chant, Microwave Enhancement of Thermal Landmine Signatures, *Proc. SPIE—Int. Soc. Opt. Eng.*, vol. 3710, no. 1, pp. 154–166, 1999.
- 15. B. A. Baertlein, K. Khanafer, and K. Vafai, Analysis and Modeling of Thermal IR Signatures of Buried Land Mines, Advanced Sensors Consortium (ASC), ARL Fourth Annual Conference, University of Maryland, College Park, pp. 263–267, 2000.
- K. Khanafer, K. Vafai, and B. A. Baertlein, Effects of Thin Metal Outer Case and Top Air Gap on Thermal IR Images of Buried Antitank and Antipersonnel Land Mines, *IEEE Trans. Geosci. Remote Sensing*, vol. 41, no. 1, pp. 123–135, 2003.
- R. L. Van Dam, B. Borchers, J. M. H. Hendrickx, and S. Hong, Soil Effects on Thermal Signatures of Buried Nonmetallic Landmines. *Proc. SPIE—Int. Soc. Opt. Eng. Detection* and Remediation Technologies for Mines and Minelike Targets VIII, Orlando, FL, April 21–25, 2003, pp. 1210–1218.
- 18. M. A. Celia, E. T. Bouloutas, and R. L. Zarba, General Mass-Conservative Numerical Solution for the Unsaturated Flow Equation, *Water Resources Res.*, vol. 26, no. 7, pp. 1483–1490, 1990.
- P. C. D. Milly, Moisture and Heat Transport in Hysteretic, Inhomogeneous Porous Media: A Matric Head-Based Formulation and a Numerical Model, *Water Resources Res.*, vol. 18, no. 3, pp. 489–498, 1982.
- 20. J. R. Philip and D. A. De Vries, Moisture Movement in Porous Materials under Temperature Gradients, *Trans. Am. Geophys. Union*, vol. 38, no. 2, pp. 222–232, 1957.
- 21. M. Deru, A Model for Ground-Coupled Heat and Mass Transfer from Buildings, Ph.D. thesis, Colorado State University, Fort Collins, CO, 2001.
- 22. H. Janssen, The Influence of Soil Moisture Transfer on Building Heat Loss via the Ground, Ph.D. thesis, Katholieke Universiteit Leuven, Leuven, Belgium, 2002.
- 23. P. J. Camillo and R. J. Gurney, A Resistance Parameter for Bare-Soil Evaporation Models, *Soil Sci.*, vol. 141, no. 2, pp. 95–105, 1986.
- 24. F. P. Incropera and D. P. DeWitt, *Fundamentals of Heat and Mass Transfer*, Wiley, New York, 2002.
- 25. W. H. McAdams, Heat Transmission, McGraw-Hill, New York, 1954.
- 26. S. V. Patankar, *Numerical Heat Transfer and Fluid Flow*, Hemisphere, McGraw-Hill, Washington, DC, New York, 1980.

- W. J. Gordon and L. C. Theil, Transfinite Mappings and Their Applications to Grid Generation, in J. F. Thompson (ed.), *Numerical Grid Generation*, pp. 171–192, North Holland, New York, 1998.
- 28. Q. Qin, P. Berliner, and A. Karnieli, Numerical Solution of a Complete Surface Energy Balance Model for Simulation of Heat Fluxes and Surface Temperature under Bare Soil Environment, *Appl. Math. Comput.*, vol. 130, pp. 171–200, 2002.
- R. Haverkamp, M. Vauclin, J. Touma, P. J. Wierenga, and G. Vachaud, Comparison of Numerical Simulation Models for One-Dimensional Infiltration, *Soil Science Society of America Journal*, vol. 41, no. 2, pp. 285–294, 1977.

APPENDIX I

A. Properties of Dry Soil and Mine Materials

Two mine materials (explosives) are used in this work, TNT and Tetryl explosives. In addition, heavy clay is used to generate the dry results. Properties of mines and dry soil are listed in Table Ia.

B. Properties of Wet Soil

Three types of soil were used in this work, Yolo light clay, sandy clay loam, and heavy clay, the properties of which are listed in Table Ib. As a special case, the hydraulic conductivity of Yolo light clay is obtained from the equation used by Haverkamp et al. [29].

C. Thermal Properties of Air, Water, and Soil Constituents

The thermal properties for air and water are listed in Table Ic.

$$k_a = 0.02417 + 7.596 * 10^{-5} (T - 273.15)$$
(I.1)

$$k_w = 0.5694 + 1.847 * 10^{-3} (T - 273.15) - 7.394 * 10^{-6} (T - 273.15)$$
 (I.2)

$$\sigma = 0.1171 - 0.0001516 T \tag{I.3}$$

Table Ia. Thermal properties of mine materials and dry soil

	$\rho (kg/m^3)$	C_p (J/kg K)	k (W/mK)
TNT	1,560	1,370	0.2234
Tetryl	1,700	1,050	0.09
Heavy clay	2,080	921	0.813

Table Ib. Types and properties of soils used in this work

Fractions			Fitted parameters						
Soil type	Sand	Silt	Clay	θ_s	θ_r	α	n	$K_{\rm sat}$	τ
Yolo light clay Sandy clay loam Heavy clay	0.238 0.56 0.2	0.4 0.16 0.1	0.442 0.28 0.7	0.495 0.433 0.415	0.1 0.0737 0.0965			1.27E-7 3.65E-6 7.07E-7	0.5 -1.02 -3.59

Table Ic. Thermal properties of air and water

	$\rho (kg/m^3)$	C_p (J/kg K)		$\sigma (J/m^2)$
Air	1.2	1,005	Eq. (I.1)	
Water	998	4,180	Eq. (I.2)	Eq. (I.3)

Table Id. Thermal and physical properties of soil constituents

	$\rho (kg/m^3)$	$C_p (\mathrm{J/kgK})$	k (W/m K)	g_a
Quartz	2,650	731.5	Eq. (I.5)	0.144
Other minerals	2,650	731.5	2.93	0.144
Organic material	1,300	1,923	0.25	0.5

where k_a , k_w , and σ are the thermal conductivity of air, thermal conductivity of water, and surface tension, respectively. The saturated vapor density is calculated using

$$\rho_{vs} = exp \left(\frac{13.873T - 3529.9}{T - 105.84} \right) \times 10^{-3} \tag{I.4}$$

Table Id shows the thermal and physical properties of soil constituents, in which $k_{\rm qtz}$ is calculated as

$$k_{\text{qtz}} = 9.051 + 0.02659(T - 273.15)$$
 (I.5)

where $k_{\rm qtz}$ is the thermal conductivity of quartz.